Computers and Geotechnics 144 (2022) 104651

Contents lists available at ScienceDirect

Computers and Geotechnics

journal homepage: www.elsevier.com/locate/compgeo

Research paper

An optimized volume of fluid method for modelling three-dimensional debris flows. Implementation in OpenFOAM, validation, and application in the Aiwa Watershed, Beijing

Yan Zhang [a,b], Liqun Lyu [a,*], Peng Li [b]

[a] School of Soil and Water Conservation, Beijing Forestry University, Beijing, 100083, China
[b] Institute of Mechanics, Chinese Academy of Sciences, Beijing, 100190, China

ARTICLE INFO

Dataset link: https://github.com/YanZhang-cas/interDebrisFoam.git

Keywords:
Debris flow
Volume of fluid
Herschel–Bulkley
Aiwa Watershed
OpenFOAM

ABSTRACT

Debris flows are a common type of geological hazard. They move down slopes at rapid speeds, causing severe damage to buildings and humans. It is of great significance to study the development and movement characteristics of debris flows. In this study, we developed a numerical method of simulating the movement of debris flows. The phase fraction was used to represent the contents of the debris flow components. The Herschel–Bulkley–Papanastasiou model was used to simulate the movement of the fine particle–water mixture in the debris flow, and the pressure-dependent Coulomb viscoplastic model was used to describe the movement of the gravel-size particles. The interface between the debris flow and the air was obtained using the volume of fluid method. The above models were implanted in OpenFOAM. Finally, indoor experimental data were used to verify the numerical method developed in this study, and the experimental and simulation results were found to be in good agreement. The proposed method was then applied to debris flow prediction in the Aiwa Watershed, Beijing. The homogeneous flow model developed in this study can significantly reduce the number of calculations required and can be used for the three-dimensional simulation of large-scale debris flows.

1. Introduction

Debris flows are a very common type of geological disaster in mountainous areas. They are composed of coupled fluid–solid materials and are the result of rainfall confluence. They move down slopes at fast speeds until they reach the accumulation area, causing significant damage to buildings and structures (Jeong and Lee, 2019). Due to their fast flow velocity, large flow volumes, sudden occurrence, and severe destructive power (Guzzetti et al., 2008; Benn et al., 2012; Allstadt et al., 2018; Shen et al., 2020; Song et al., 2021), once a debris flow is formed, it can reach the downstream area in a very short period of time, resulting in a very limited response time for the people living downstream. Debris flows can suddenly cause high casualties and property loss in downstream villages. The formation of debris flows is complicated as it is difficult to predict and is affected by various factors, such as geological structures, meteorology, hydrology, topography, and human activities. Because of their clustered occurrence and periodic characteristics, debris flows have received extensive attention worldwide.

Previous studies of debris flows have mainly focused on the formation conditions, movement characteristics, and development trends of debris flows. In particular, studying the movement characteristics and development trends of debris flows is of great value. Indoor experiments have often been used in these studies (Toniolo et al., 2004; Lu et al., 2016; Goodwin and Choi, 2020; Walczak et al., 2021), yet the scale of these experiments is often limited. Due to the size effect of indoor experiments, whether they can reflect the actual movement of a debris flow is still unknown (von Boetticher et al., 2016). In addition, the measurement method used in indoor experiments is also limited. Only macroscopic data such as the movement speed, form, and height of the granular column can be measured, and it is impossible to characterize the internal interactions. Compared with experimental methods, numerical simulations are more advantageous in investigating the movement characteristics and development trends of debris flows. It is possible to obtain detailed information using numerical simulations that cannot be obtained from experiments. Moreover, the cost of numerical simulations is much lower than that of experiments. However, numerical simulations are not without limitations. First, the simulation is greatly dependent on the values of the relative parameters, such as the physical parameters, rheological model, and topographic data. The accuracy of these parameters directly affects the quality of the

* Corresponding author.
E-mail address: lvliqun@bjfu.edu.cn (L. Lyu).

https://doi.org/10.1016/j.compgeo.2022.104651
Received 4 September 2021; Received in revised form 30 December 2021; Accepted 19 January 2022
Available online 8 February 2022
0266-352X/© 2022 Elsevier Ltd. All rights reserved.

simulation results. Moreover, numerical simulations of debris flows on the actual scale can result in a massive calculation cost. Thus, the depth-averaged method is often used to simplify the flow equation, and only 1-D (Imran et al., 2001) or 2-D (Li et al., 2013; Qian and Das, 2019; Takebayashi and Fujita, 2020) problems are simulated. However, these models are one-dimensional or two-dimensional simplifications of the Navier–Stokes-type equations and neglect the nonlinear behaviour of the debris flow in the depth direction (Han et al., 2015b). By assuming that a debris flow is a Bingham body, Huang and García (1997) derived the motion equation for a one-dimensional debris flow. It was also found that it is not appropriate to assume that a debris flow is a Newtonian fluid. Based on this model, Imran et al. (2001) studied the influences of the initial column on the velocity and distance of a 1-D debris flow.

To acquire a full description of the debris flow, full 3-D modelling is suitable, even though it has a high computational cost (Adebiyi and Hu, 2021). Zhang et al. (2021c) used a eulerian–eulerian three-dimensional two-phase model to describe the motion of submarine debris flows, in which the kinetic theory of granular flow is employed for the solid stress and viscosity. The smoothed particle hydrodynamic (SPH) (Tayyebi et al., 2021) method is another approach for 3-D debris flow modelling, in which the continuum fluid is treated as a set of discretized particles (Liang et al., 2015). However, the SPH method is not suitable when the topography changes abruptly, such as flow obstacles. It is also less valid when there are strong gradients in the debris flow, such as flow initiation and deposition. A coupled computational fluid dynamics and discrete element method (CFD-DEM) has also been used to study the motion of debris flows, such as the impact of the solid fraction (Li and Zhao, 2018; Lee et al., 2019; Li et al., 2020b; Fang et al., 2021; Kong et al., 2021). Since it takes a long time to track particles using this method, the computational requirement is expensive. Therefore, it is not suitable for the simulation of actual three-dimensional debris flows. The components of a debris flow usually include clay, silt, sand, gravel, and interstitial water. When the gravel content is small, a large amount of clay results in a high viscosity, and the equivalent fluid assumption can be used. The volume of fluid (VOF)-based method has also been used in 3-D debris flow modelling. Usually, the debris flow is seen as a uniform mixture. For example, Zhao et al. (2021) investigated the effect of submarine debris flow on pipelines, where the debris flow is set as slurry. Zhang et al. (2021b) proposed a VOF-based model for three-dimensional debris flow, where the debris flow mixture is also regarded as slurry. Similar work is also taken by Yu et al. (2020). von Boetticher et al. (2016) developed a VOF model for three-dimensional debris flow by considering the different materials in a debris flow mixture, such as the granular component and interstitial fluid component. However, for the considerations of computational efficiency, they neglected phase interactions.

Generally, when the concentration of solids in a debris flow is greater than 10%, the debris flow will exhibit non-Newtonian fluid characteristics (Pastor et al., 2014; Song et al., 2017; Li and Zhao, 2018; Yu et al., 2020). Several studies have regarded debris flows as uniform non-Newtonian fluids based on the equivalence assumption and have used the Bingham model or Herschel–Bulkley (H–B) model to describe the rheological properties (Dai et al., 2014; Han et al., 2015a; Song et al., 2017; Kang and Kim, 2017; Pang et al., 2018; sen Guo et al., 2019; Zhang et al., 2021c). However, when the gravel content of the debris flow is large, the equivalence hypothesis can produce larger errors (von Boetticher et al., 2016; Yang et al., 2020). Therefore, the gravel in the debris flow should be considered separately. In this study, we mainly focused on the movement characteristics of debris flows with large gravel contents. The mixture of interstitial water and soil (clay, silt, and sand) was regarded as a slurry and was described using the H–B model. The gravel was described using the pressure-dependent Coulomb viscoplastic model (Domnik et al., 2013). Considering the calculation cost and accuracy of the movement characteristics of debris flows, the homogeneous flow model was used to simulate a debris flow; that is, the phase fraction was used to represent the content of each component of the debris flow (slurry phase and gravel phase). The interaction between the slurry and the gravels, such as the drag force, is considered based on the velocity slip between the two phases. The interface between the debris flow and the air was defined as a free interface, and the VOF method was used to capture the free surface. The amount of computation required for this method is moderate; thus, it is suitable for the numerical simulation of the three-dimensional movement of large-scale debris flows. The models were implanted in OpenFOAM as a new solver *interDebrisFoam* and then applied to experimental cases for model verification. The model was also applied to a field case in the Longtangou Watershed, Beijing, to study the motion of a large-scale debris flow.

2. Methods

InterFoam (Duy et al., 2021) is a well-established solver for simulations of flows in which two immiscible fluids are present. A distinct surface interface can be defined based on the VOF method in OpenFOAM, which is a free, open-source, parallel processing software backed by a large user-driven support community (Jasak et al., 2007; Zhang et al., 2021e). The different phases are represented in the domain in terms of their phase fractions using the VOF method. The VOF method can significantly lower computational costs. However, some field information about the two-phase flow is lost by averaging the phases (Friedemann et al., 2021). An algebraic VOF method is used in the *interFoam* solver, which is a modified version of the traditional VOF method of Hirt and Nichols (1981). *InterMixingFoam*, which was inherited from the original *interFoam* solver, is a solver for three incompressible fluids, two of which are miscible, that uses the VOF method to capture the interface (Xu et al., 2016). For example, slurry and gravels are mixed in debris flows, and there is an interface between the mixture and air. Therefore, *interMixingFoam* is more suitable. However, there is no suitable constitutive model in OpenFOAM to describe the movement of a slurry and gravels, so it is necessary to embed algorithms. The equations, algorithm, and constitutive model used in this study are presented below.

2.1. Model equations

According to Bohorquez (2012), Damián and Nigro (2014), the mixture model or the algebraic slip mixture model is a multiphase model for n interpenetrated phases based on the multifluid model (Li et al., 2019b). The continuity equations in the multifluid model for each phase are

$$\begin{cases} \frac{\partial \alpha_a \rho_a}{\partial t} + \nabla \cdot \left(\alpha_a \rho_a \mathbf{U}_a\right) = 0 \\ \frac{\partial \alpha_g \rho_g}{\partial t} + \nabla \cdot \left(\alpha_g \rho_g \mathbf{U}_g\right) = 0 \\ \frac{\partial \alpha_s \rho_s}{\partial t} + \nabla \cdot \left(\alpha_s \rho_s \mathbf{U}_s\right) = 0 \end{cases}, \tag{1}$$

where α_a, α_g, and α_s are the volume fractions of the air, gravels, and slurry, respectively, which satisfy the relationship $\alpha_a+\alpha_g+\alpha_s = 1$. ρ_a, ρ_g, and ρ_s are the densities of the air, gravels, and slurry, respectively. $\mathbf{U}_a$, $\mathbf{U}_g$ and $\mathbf{U}_s$ are the velocities of the air, gravels, and slurry, respectively. Dividing the three equations in Eq. (1) by the phase density and adding the three resulting equations yields

$$\nabla \cdot \mathbf{u} = 0, \tag{2}$$

where $\mathbf{u} = \alpha_a \mathbf{U}_a + \alpha_g \mathbf{U}_g + \alpha_s \mathbf{U}_s$ is the volumetric velocity.

The momentum balance equations of each phase can be written as

$$\begin{cases} \frac{\partial \alpha_a \rho_a \mathbf{U}_a}{\partial t} + \nabla \cdot \left(\alpha_a \rho_a \mathbf{U}_a \mathbf{U}_a\right) - \nabla \cdot \left(\alpha_a \tau_a\right) = \alpha_a \rho_a \mathbf{g} - \nabla P_a \\ \frac{\partial \alpha_g \rho_g \mathbf{U}_g}{\partial t} + \nabla \cdot \left(\alpha_g \rho_g \mathbf{U}_g \mathbf{U}_g\right) - \nabla \cdot \left(\alpha_g \tau_g\right) = \alpha_g \rho_g \mathbf{g} - \alpha_g \nabla P_g - \mathbf{F} \\ \frac{\partial \alpha_s \rho_s \mathbf{U}_s}{\partial t} + \nabla \cdot \left(\alpha_s \rho_s \mathbf{U}_s \mathbf{U}_s\right) - \nabla \cdot \left(\alpha_s \tau_s\right) = \alpha_s \rho_s \mathbf{g} - \alpha_s \nabla P_s + \mathbf{F} \end{cases}, \tag{3}$$

where P_a, P_g, and P_s are the phase pressure of the air, gravels, and slurry, τ_a, τ_g, and τ_s are the shear stress of the three phases, $\mathbf{g}$ is the acceleration due to gravity, and $\mathbf{F}$ is the interaction force between the slurry and the gravels. Adding the three equations in Eq. (3) yields

$$\frac{\partial \rho \mathbf{U}}{\partial t} + \nabla \cdot (\rho \mathbf{U}\mathbf{U}) - \nabla \cdot \left(\boldsymbol{\tau} + \boldsymbol{\tau}_{\mathbf{m}}\right) = -\nabla P + \rho \mathbf{g} , \tag{4}$$

where $\rho = \alpha_a\rho_a + \alpha_g\rho_g + \alpha_s\rho_s$ is the mixture density, $\mathbf{U}$ is the mass-average velocity

$$\begin{aligned} \mathbf{U} &= \frac{1}{\rho}\left(\alpha_a\rho_a\mathbf{U}_a + \alpha_g\rho_g\mathbf{U}_g + \alpha_s\rho_s\mathbf{U}_s\right) \\ &= \mathbf{u} + \alpha_g\left(1-\alpha_g\right)\frac{\rho_g - \rho_s}{\rho}\mathbf{U}_{gs} , \end{aligned} \tag{5}$$

where $\mathbf{U}_{gs}$ is the relative velocity of the gravels with respect to the slurry, which can be expressed as Damián and Nigro (2014)

$$\mathbf{U}_{gs} = \mathbf{U}_r\left(1-\alpha_g\right)^a \tag{6}$$

where $\mathbf{U}_r$ and a are constants. $\mathbf{U}_r$ can be regarded as the average settling velocity of solid particles in still liquid

$$\mathbf{U}_r = \frac{d^2}{18\mu_s}(1-\alpha_g)^5(\rho_g - \rho_s)\mathbf{g} , \tag{7}$$

where d is the particle diameter and μ_s is the slurry viscosity. P is the mixture pressure, which is given by

$$P = P_a + P_g + P_s , \tag{8}$$

τ is the bulk stress tensor

$$\tau = \alpha_a\tau_a + \alpha_g\tau_g + \alpha_s\tau_s , \tag{9}$$

τ_m is the tensor representing the interaction due to the relative motion of gravels with respect to the slurry

$$\tau_m = -\alpha_g\left(1-\alpha_s\right)\frac{\rho_s\rho_g}{\rho_m}\mathbf{U}_{gs}\mathbf{U}_{gs} , \tag{10}$$

where $\rho_m = \alpha_g\rho_g + \alpha_s\rho_s$ is the mixture density of the gravels and the slurry.

The mixture pressure consists of two parts: the static pressure and the dynamic pressure. When a large static pressure exists in a certain physical problem, the calculation may produce a false velocity due to hydrostatic pressure. Moreover, it is complicated when defining the boundary conditions under which the boundary pressure changes with height. Therefore, the pressure gradient term in Eq. (4) is changed to the following form (Berberović et al., 2009):

$$P = P_{rgh} + \rho\mathbf{g}\cdot\mathbf{h} , \tag{11}$$

$$\nabla P = \nabla P_{rgh} + \mathbf{g}\cdot\mathbf{h}\nabla\rho + \rho\mathbf{g} , \tag{12}$$

where P_{rgh} is the dynamic pressure and $\mathbf{h}$ is the position vector. By substituting Eq. (12) into Eq. (4), we obtain (considering the surface tension force)

$$\frac{\partial \rho \mathbf{U}}{\partial t} + \nabla \cdot (\rho \mathbf{U}\mathbf{U}) - \nabla \cdot (\boldsymbol{\tau} + \tau_m) = -\nabla P_{rgh} - \mathbf{g}\cdot\mathbf{h}\nabla\rho + \sigma\kappa\nabla\alpha . \tag{13}$$

The viscosity stress tensor term in Eq. (13) can be written as follows:

$$\nabla\cdot\boldsymbol{\tau} = \nabla\cdot\left(\mu\left(\nabla\mathbf{U} + \nabla\mathbf{U}^{\mathrm{T}}\right)\right) = \nabla\cdot(\mu\nabla\mathbf{U}) + \nabla\mathbf{U}\cdot\nabla\mu , \tag{14}$$

where the superscript T denotes the transpose. By substituting Eq. (14) into Eq. (13), we obtain

$$\frac{\partial \rho \mathbf{U}}{\partial t} + \nabla\cdot(\rho\mathbf{U}\mathbf{U}) - \nabla\cdot(\mu\nabla\mathbf{U}) - \nabla\mathbf{U}\cdot\nabla\mu - \nabla\cdot\tau_m = -\nabla P_{rgh} - \mathbf{g}\cdot\mathbf{h}\nabla\rho + \sigma\kappa\nabla\alpha . \tag{15}$$

Dividing the continuity equation of the air in Eq. (1) by ρ_a yields

$$\frac{\partial \alpha_a}{\partial t} + \nabla\cdot\left(\alpha_a\mathbf{U}_a\right) = 0 . \tag{16}$$

Because the air is immiscible with respect to the mixture of slurry and the gravels, α_a defines the interface between the air and the mixture (gravels and slurry). The volumetric velocity can be rewritten as

$$\mathbf{u} = \alpha_a\mathbf{U}_a + (1-\alpha_a)\mathbf{u}_m , \tag{17}$$

where $\mathbf{u}_m = \alpha_g\mathbf{U}_g + \alpha_s\mathbf{U}_s$ is the volumetric velocity of the mixture of the gravels and the slurry. Only the interaction between the slurry and the gravels is considered. As a results, it is assumed that $\mathbf{u}_m = \mathbf{U}_a$. Eq. (16) can be written as

$$\frac{\partial \alpha_a}{\partial t} + \nabla\cdot\left(\alpha_a\mathbf{u}\right) = 0 . \tag{18}$$

The value of the phase fraction of the air should be 0 or 1. The method proposed by Weller (2002) was implemented in OpenFOAM. Specifically, an artificial convection term was added to squeeze the phase fraction near the interface to counteract the ambiguity of the phase interface caused by numerical dissipation. The artificial convection term must be zero outside of the phase interface. Therefore, the VOF model of the air phase can be expressed as (Albadawi et al., 2013)

$$\frac{\partial \alpha_a}{\partial t} + \nabla\cdot\left(\alpha_a\mathbf{u}\right) + \nabla\cdot\left(\alpha_a(1-\alpha_a)c|\mathbf{u}|\frac{\nabla\alpha_a}{|\nabla\alpha_a|}\right) = 0 , \tag{19}$$

where c is a controllable compression factor; when $c = 0$, there is no compression. The larger c is, the faster and more obvious the compression is. In addition, the boundedness of the volume fraction is guaranteed by the Multidimensional Universal Limiter with Explicit Solution (MULES) algorithm, which is a flux corrected transport-based scheme (Zalesak, 1979). Detailed descriptions of the numerical schemes and the implementation of the MULES algorithm in the *interFoam* program in OpenFOAM can be found in Deshpande et al. (2012) and Nguyen Duy and Hino (2020).

The gravels velocity $\mathbf{U}_g$ can be derived as

$$\mathbf{U}_g = \mathbf{u} + (1-\alpha_s)\mathbf{U}_{gs} , \tag{20}$$

Similar to the continuity equation of the air, dividing the continuity equation of the gravels in Eq. (1) and considering the diffusion between the gravels and slurry yields

$$\frac{\partial \alpha_g}{\partial t} + \nabla\cdot\left(\alpha_g\mathbf{u}\right) + \nabla\cdot\left[\alpha_g(1-\alpha_g)\mathbf{U}_{gs}\right] - D_{gs}\nabla^2\alpha_g = 0 . \tag{21}$$

where D_{gs} is the diffusion coefficient between the slurry and the gravel phases, and a small value (1×10^{-6}) was used in this study. By solving Eqs. (16) and (21), the phase fractions of the air and gravels can be obtained. Then, according to $\alpha_s = 1 - \alpha_a - \alpha_g$, the phase fraction of the slurry is obtained. A cell-centre-based finite volume method (FVM) incorporating the finite volume approximation of the transport equations was used in this study. The transient terms were evaluated using the first-order implicit Euler scheme, and the convective and diffusion terms were discretized using a second-order resolution scheme. The pressure was coupled with the velocity using the pressure implicit with splitting of operators (PISO) algorithm (Issa et al., 1986). The Courant number was set to less than 1 to prevent numerical errors.

2.2. Solution procedure

The normal flux of α_a and α_s at cell face is

$$\begin{aligned} \phi_a &= \left(\alpha_a\mathbf{u} + \alpha_g\alpha_a c|\mathbf{u}|\frac{\nabla\alpha_a}{|\nabla\alpha_a|} + \alpha_s\alpha_a c|\mathbf{u}|\frac{\nabla\alpha_a}{|\nabla\alpha_a|}\right)_f\cdot\mathbf{S}_f \\ &= \alpha_{af}\phi_u + \alpha_{gf}\alpha_{af}\phi_r + \alpha_{sf}\alpha_{af}\phi_r , \end{aligned} \tag{22}$$

$$\begin{aligned} \phi_s &= \left[\alpha_g\mathbf{u} + \alpha_g(1-\alpha_g)\mathbf{U}_{gs}\right]_f\cdot\mathbf{S}_f \\ &= \alpha_{gf}\phi_u + \alpha_{gf}(1-\alpha_{gf})\phi_{gs} \end{aligned} \tag{23}$$

where $\phi_u = \mathbf{u}_f\cdot\mathbf{S}_f$ is the normal flux of the volumetric velocity $\mathbf{u}$, $\phi_r = c|\mathbf{u}|(\frac{\nabla\alpha_a}{|\nabla\alpha_a|})_f\cdot\mathbf{S}_f$, $\phi_{gs} = \mathbf{U}_{gs}\cdot\mathbf{S}_f$, $\mathbf{u}_f$ is the volumetric velocity at the cell face f, $\mathbf{S}_f$ is the exterior normal vector of the cell face, and subscript f represents the value at the cell face. Eqs. (19) and (21) can be solved based on the MULES algorithm. The normal mass flux at the cell face can be calculated by

$$\rho\phi = \alpha_a\phi_a\left(\rho_a - \rho_s\right) + \phi_s\left(\rho_g - \rho_s\right) + \phi_u\rho_s , \tag{24}$$

where ϕ is the normal flux of the mass-average velocity $\mathbf{U}$. The semi-discretized form of the momentum equation (15) can be written as Zhang et al. (2021d)

$$A_P\mathbf{U}_P^*+\sum A_N\mathbf{U}_N^*-S_P^n=\mathbf{C}(P_{\mathrm{rgh},P}P_{\mathrm{rgh},N})+\mathbf{E}_P\,, \tag{25}$$

where A_P is a coefficient related to the current element P, A_N is a coefficient related to the adjacent element N, $\mathbf{U}_P^*$ is the predicted mass-average velocity at the centre point of element P, the superscript n denotes the n_{th} time step, $*$ is the momentum prediction, and the subscripts P and N denote the two elements. $\mathbf{C}(P_{\mathrm{rgh},P}, P_{\mathrm{rgh},N})$ denotes the discrete form of the pressure gradient term, and $\mathbf{E}_P$ is the discrete form of the volume force and the surface tensor term. By solving Eq. (25), the predicted mass-average velocity can be obtained, but it does not satisfy the continuity equation. Based on the convergence situation, Eq. (2) is discretized as follows:

$$\sum\left(\mathbf{u}_f^{n+1}\cdot\mathbf{S}_f\right)=0\,, \tag{26}$$

where $\mathbf{u}_f^{n+1}$ is the volumetric velocity at the cell face f at time $n+1$. According to Eq. (5), Eq. (26) can be rewritten as

$$\sum\left[\mathbf{U}_f\cdot\mathbf{S}_f-\alpha_{\mathrm{g}}(1-\alpha_{\mathrm{g}})\frac{\rho_{\mathrm{g}}-\rho_{\mathrm{s}}}{\rho}\phi_{\mathrm{gs}}\right]=0 \tag{27}$$

At convergence, Eq. (25) can be written as

$$A_P\mathbf{U}_P^{n+1}+\sum A_N\mathbf{U}_N^{n+1}-S_P^n=-\nabla P_{\mathrm{rgh},P}^{n+1}-\mathbf{g}\cdot\mathbf{h}\nabla\rho_P^{n+1}+\sigma\kappa\nabla\alpha_P^{n+1}\,, \tag{28}$$

Let

$$\mathbf{HbyA}_P^{n+1}=\frac{1}{A_P}\left(-\sum A_N\mathbf{U}_N^{n+1}+S_P^n\right)\,. \tag{29}$$

It follows that Eq. (28) can be rewritten as

$$\mathbf{U}_P^{n+1}=\mathbf{HbyA}_P^{n+1}-\frac{1}{A_P}\left(\nabla P_{\mathrm{rgh},P}^{n+1}+\mathbf{g}\cdot\mathbf{h}\nabla\rho_P^{n+1}-\sigma\kappa\nabla\alpha_P^{n+1}\right)\,, \tag{30}$$

where $\mathbf{HbyA}_P^{n+1}$ is the finite volume representation of the spatial convective and diffusive fluxes of the phase momentum (Jasak, 1996). According to Rhie–Chow interpolation (Rhie and Chow, 1983), the velocity on the cell face f is

$$\mathbf{U}_{P,f}^{n+1}=\mathbf{HbyA}_{P,f}^{n+1}-\frac{1}{A_{P,f}}\left(\nabla_f P_{\mathrm{rgh},P}^{n+1}+\mathbf{g}\cdot\mathbf{h}\nabla_f\rho_P^{n+1}-\sigma\kappa\nabla_f\alpha_P^{n+1}\right)\,, \tag{31}$$

By substituting Eq. (31) into Eq. (27), we obtain

$$\begin{aligned}&\sum\left(\mathbf{HbyA}_{P,f}^{n+1}+\frac{1}{A_{P,f}}\left(\sigma\kappa\nabla_f\alpha_P^{n+1}-\mathbf{g}\cdot\mathbf{h}\nabla_f\rho_P^{n+1}\right)\right)\cdot\mathbf{S}_f\\&-\sum\alpha_{\mathrm{g}}(1-\alpha_{\mathrm{g}})\frac{\rho_{\mathrm{g}}-\rho_{\mathrm{s}}}{\rho}\phi_{\mathrm{gs}}=\sum\frac{1}{A_{P,f}}\left(\nabla_f P_{\mathrm{rgh},P}^{n+1}\right)\cdot\mathbf{S}_f\,.\end{aligned} \tag{32}$$

Eq. (32) is the Poisson pressure equation. The convergent pressure can be obtained by solving this equation. After Eq. (32) is solved, ϕ_{u} can be updated as

$$\phi_{\mathrm{u}}=\phi-\alpha_{\mathrm{g}}(1-\alpha_{\mathrm{g}})\frac{\rho_{\mathrm{g}}-\rho_{\mathrm{s}}}{\rho}\phi_{\mathrm{gs}}\,. \tag{33}$$

2.3. Rheological behaviour of the slurry

In this study, the slurry was regarded as a non-Newtonian fluid, and its rheological properties can be described by the H–B model, which is characterized by a nonzero shear stress when the strain rate is zero (Han et al., 2015a; Kang and Kim, 2017). The H–B model can be represented by the following constitutive equation:

$$\tau_{\mathrm{s}}=\tau_0+k\times\dot{\gamma}^n\,, \tag{34}$$

where τ_0 is the yield stress, which is defined as the minimum shear stress required to initiate flow, k is the consistency index of the slurry, and n is the flow index of the slurry. $n\geq 1$ gives a shear-thickening slurry, while $n\leq 1$ corresponds to a shear-thinning slurry. $n=1$ leads to the Bingham model (Pang et al., 2018). $\dot{\gamma}$ is the shear rate, which is a function of the second invariant of the deformation tensor $\mathbf{D}$:

$$\dot{\gamma}=\sqrt{2\mathbf{D}:\mathbf{D}}\,, \tag{35}$$

$$\mathbf{D}=\frac{1}{2}\left(\nabla\mathbf{U}+(\nabla\mathbf{U})^{\mathrm{T}}\right)\,. \tag{36}$$

The apparent viscosity of the slurry can be expressed as follows:

$$\mu_{\mathrm{s,app}}=\frac{\tau_0}{\dot{\gamma}}+k\times\dot{\gamma}^{n-1}\,, \tag{37}$$

Based on Eq. (37), when the shear rate $\dot{\gamma}$ is close to 0, the apparent viscosity of the slurry tends to infinity. This means that from the physical perspective, the slurry does not deform in the nonregional area. However, it causes divergence or even crashes during the solution procedure in the numerical calculation (Han et al., 2019). To solve this problem, an upper limit of the apparent viscosity of the slurry is usually set, i.e., $\mu_{\max}$ (Huang et al., 2012), such that

$$\mu_{\mathrm{s,app}}=\begin{cases}\frac{\tau_0}{\dot{\gamma}}+k\times\dot{\gamma}^{n-1} & \mu_{\mathrm{s,app}}<\mu_{\max}\\ \mu_{\max} & \mu_{\mathrm{s,app}}\geqslant\mu_{\max}\end{cases}\,. \tag{38}$$

However, the selection of the value of $\mu_{\max}$ is a problem. Thus, this method has limitations. To accurately describe the movement of a debris flow under a large strain while avoiding the limitations of the H–B model, the model proposed by Papanastasiou (1987) was used to describe the rheological properties of the slurry. The model is referred to as the Herschel–Bulkley–Papanastasiou (H–B–P) model in this paper. Thus, the apparent viscosity of the slurry can be expressed as:

$$\mu_{\mathrm{s,app}}=\frac{\tau_0}{\dot{\gamma}}\left[1-\exp(-m\dot{\gamma})\right]+k\times\dot{\gamma}^{n-1}\,, \tag{39}$$

where m (constant) is the stress growth parameter. As a result, when the shear rate is small, the shear stress τ is allowed to exceed the yield stress τ_0. When $\dot{\gamma}$ is 0, $\left[1-\exp(-m\dot{\gamma})\right]/\dot{\gamma}$ in Eq. (39) is close to m, and when m is close to infinity, the Herschel–Bulkley–Papanastasiou (H–B–P) model is fully equivalent to the ideal H–B model. Fig. 1 shows the influences of parameters m and n in Eq. (39) on the H–B–P model, where $\tau_0=20$ Pa, $n=2$, and $k=1$ Pa · s. The H–B–P model converges to a certain value when the shear rate is low, and thus, there is no numerical divergence. Moreover, the H–B–P model is smooth and continuous. The convergence value and convergence speed of the apparent viscosity are determined by the value of m. The larger the value of m is, the faster the convergence is. When the value of m is large, the H–B–P model is close to the H–B model (Fig. 1(b)). The H–B–P model avoids the problem that the apparent viscosity tends to infinity when the shear rate is small. In summary, m in the H–B–P model mainly controls the rate of change of the shear stress in the plastic yield transition section with shear rate, as well as the convergence speed and value of the apparent viscosity at small shear rates. n mainly controls the nonlinear relationship between the shear stress and the shear rate under large deformations. The H–B–P model has good convergence performance and can more comprehensively reflect the complex relationship between the shear stress and the shear rate under large deformations. The regularized H–B–P model without numerical divergence was implemented in OpenFOAM.

There are four parameters in the H–B–P model that need to be determined: the yield stress τ_0, consistency index k, flow index n, and stress growth parameter m. The H–B parameters of the slurry can be linked to the properties of the slurry, such as the solid volumetric concentration, the clay percentage, and the clay type, which can be measured via geotechnical tests. The materials in a debris flow were tested by Coussot et al. (1998). They found that $n=1/3$ for the different mixtures, while k and τ_0 increase roughly proportionally as the concentration of the solids increases. Nguyen et al. (2018) showed that when the clay fraction of the slurry is less than 30%, the slurry can be described by the Bingham model, that is, $n=1$. In addition, based on physical experiments, they determined the relationship between the

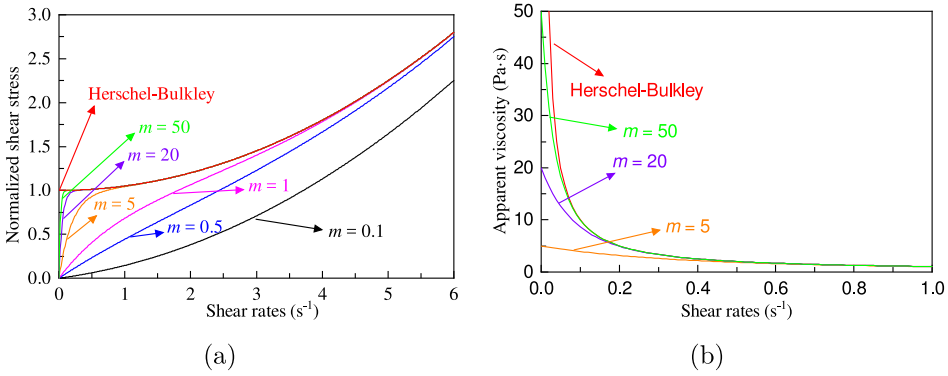

Fig. 1. (a) Influence of m on the stress in the H–B–P model. (b) Influence of m on the apparent viscosity in the H–B–P model. τ_0 = 20 Pa, n = 2, and k = 1 Pa·s.

yield stress τ_0 and the clay fraction and water content in the Bingham model.

$$\tau_0 = 3.504 \exp\left(2327.2 \frac{C_F}{w^{2.78}}\right), \tag{40}$$

where C_F is the clay fraction, which ranges from 5% to 30%, and w is the water content. Considering the simplicity of the model proposed by Nguyen et al. (2018), this model was used in this study. As seen from Fig. 1, when $m \geq 5$, the H–B–P model is close to the H–B model.

2.4. Rheological behaviour of the gravel

In the previous section, the rheological behaviour of the slurry (a mixture of fine particles and water) in the debris flow was analysed, and the values of the model parameters were given. In this section, we introduce the rheological behaviour of gravel. When there is much gravel in the debris flow, the equivalence hypothesis is not reasonable, and the gravel in the debris flow needs to be considered separately (von Boetticher et al., 2016; Yang et al., 2020). Since there is no cohesion between gravel particles, it can be regarded as granular flow. The motion and settling of dry granular materials can be described well by viscoplastic constitutive laws (Jop et al., 2006; Forterre and Pouliquen, 2008; Domnik and Pudasaini, 2012). Domnik et al. (2013) developed a full two-dimensional Coulomb-viscoplastic model, which includes the basic features of granular flow, such as the exhibition of a yield strength and a nonzero slip velocity. The frictional nature of granular materials is accounted for by the pressure-dependent yield strength, which is related to the internal friction angle of the materials. The stress tensor for a viscoplastic flow can be written as:

$$\boldsymbol{\tau}_g = -P\mathbf{I} + 2\mu_{g,eff}\mathbf{D}, \tag{41}$$

where P is the mixture pressure, $\mathbf{I}$ is a unit tensor, and $\mu_{g,eff}$ is the apparent viscosity of the gravel, which can be expressed as:

$$\mu_{g,eff} = \mu_g + \frac{\tau_0'}{\|\mathbf{D}\|}, \tag{42}$$

$$\tau_0' = P\sin(\theta), \tag{43}$$

where μ_g is the constant dynamic viscosity, τ_0' is the yield stress of the gravel, $\|\mathbf{D}\| = \sqrt{2tr(\mathbf{D}^2)}$ is the norm of the deformation tensor, and θ is the internal friction angle of the gravel, which describes the friction between the gravels. The gravel acts as a Newtonian fluid when $\tau_0' = 0$. The yield stress τ_0' is significant to the transition of the gravel between the solid state and the fluid state in response to the flow initiation and deposition processes. The pressure dependence of the yield stress (Eq. (43)) causes higher resistance against deformation in high-pressure regions. Similar to the H–B model, when $\|\mathbf{D}\|$ is close to 0, $\mu_{g,eff}$ tends to infinity, leading to calculation divergence. Therefore, a method similar to that used in the previous section was adopted (Papanastasiou, 1987), and an exponential growth parameter s with a dimension of time was introduced in this study:

$$\mu_{g,eff} = \mu + \frac{P\sin(\theta)}{\|\mathbf{D}\|}\left[1 - \exp(-s\|\mathbf{D}\|)\right], \tag{44}$$

Eq. (44) is uniform in the unyielding and yielding regions, and the transition between these regions is smoother for smaller values of s (Papanastasiou, 1987). Fig. 2 shows the influences of parameters s, P, and θ in Eq. (44) on the Coulomb-viscoplastic model, where $\mu = 0.01\text{Pa}\cdot\text{s}$. As the norm of the deformation tensor increases, the apparent viscosity of the gravel decreases significantly. The greater the pressure is, and the smaller the normal vector of the deformation tensor is, the larger the apparent viscosity is. That is, at places close to the wall, because the pressure is large and $\|\mathbf{D}\|$ is small, the velocity of the column will be more likely to decrease, causing the debris flow to stop, which is consistent with the actual situation. However, when the shear rate is large, the apparent viscosity of the gravel is small; thus, the contribution of the gravel in the debris flow is reduced, and it is carried forward by the slurry. In addition, the internal friction angle also has a significant effect on the apparent viscosity. The larger the internal friction angle is, the larger the apparent viscosity of the gravel and the faster the convergence of the Coulomb-viscoplastic model. The internal friction angle can be obtained through experiments. Generally, the internal friction angle of gravel is approximately 30°. According to Fig. 2(c), as s increases, the apparent viscosity decreases when $\|\mathbf{D}\| < 10$. When $\|\mathbf{D}\| \geq 10$, the apparent viscosity remains constant. The value of s is set as 1.0 to ensure that, in the absence of shear, the apparent viscosity will achieve a viscosity representing Coulomb friction with a sole dependence on the normal pressure.

3. Numerical verification

In this section, three examples are used to verify the effectiveness of the proposed method (*interDebrisFoam*). First, the flow between two parallel plates was tested to validate the implementation of the H–B–P model in the present work in OpenFOAM. Then, a granular column collapse experiment was carried out to verify the applicability of the Coulomb-viscoplastic model. Finally, the applicability of the entire method was verified using a debris flow experiment.

3.1. Flow between two parallel plates

As shown in Fig. 3, there is flow between two plates. The flow is described by the Bingham model (n = 1 in the H–B model). When the pressure difference is known, the velocity distribution of the flow between the plates is (Gopala et al., 2011)

$$U(y) = \begin{cases} \frac{\Delta P H}{2kL}\left(y - \frac{y^2}{H}\right) - \frac{\tau_0 y}{k} & 0 \leq y \leq h \\ U(h) & h < y \leq \frac{1}{2}H \end{cases}, \tag{45}$$

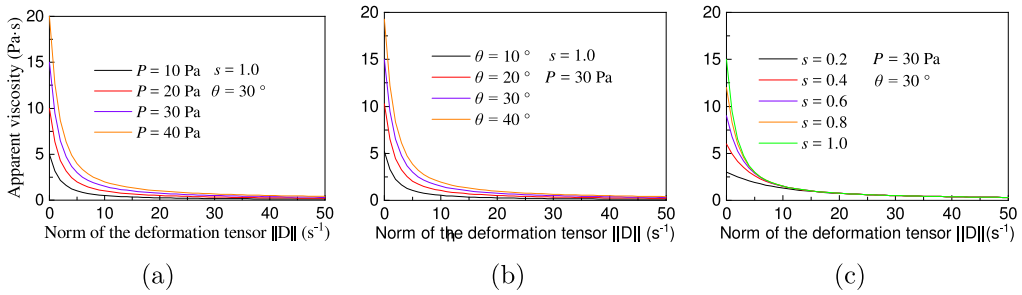

Fig. 2. The change in the apparent viscosity $\mu_{g,eff}$ with the norm of deformation tensor $\|\mathbf{D}\|$, (a) effect of pressure P, (b) effect of internal friction angle θ, and (c) effect of exponential growth parameter s.

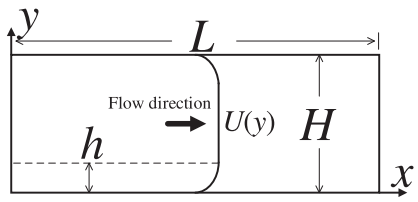

Fig. 3. Schematic diagram of the flow between two plates.

Table 1
Rheological parameters of the simulated H–B–P fluid.

Parameters	SCC	Grout
Density (kg/m^3)	2200	1900
Yield stress τ_0 (Pa)	131	2
Consistency index k (Pa·s)	44.9	11
Flow index n	1	1
Stress growth parameter m (s)	5	5

where L is the length of the plates, H is the clearance between the plates, h is the height below the plug zone, k is the consistency index in Eq. (38), and ΔP is the pressure difference. The size of the plug between the two plates is calculated as $2\tau_0 L/\Delta P$ (Gopala et al., 2011). The $h = 0.5(H - 2\tau_0 L/\Delta P)$. In this study, a two-dimensional plate with a length of $L = 2$ m and a height of $H = 0.1$ m was modelled. The shape of the plate was the same as in Fig. 3. The numbers of elements in the x and y directions were 150 and 25, respectively. The fluid velocity at the upper and lower walls was 0 m/s, the pressure gradient was 0 Pa/m, the velocity at the left entrance was 0.069 m/s (Gopala et al., 2011), with a pressure gradient of 0 Pa/m, the velocity gradient at the right exit was 0 (m/s)/m, and the pressure was 0 Pa. In the beginning, the field was filled with fluids with a velocity of 0 m/s. Two types of fluids were used in the simulation, namely, a self-compacting cement (SCC) mixture and grout. The parameters of the two fluids were the same as those used by Gopala et al. (2011), as shown in Table 1.

Fig. 4 shows the velocity (along the x direction at the cross-section of the $x = 1$ m) distribution calculated using the proposed method and that obtained from Eq. (45). It was found that the results are in good agreement. The width of the plug area ($H - 2h$) of the SCC is approximately 0.04 m, and that of the grout is approximately 0.01 m. Therefore, the velocity profile of the SCC is very different from that of the grout. This is due to the greater strength of the SCC. The shear rate in the middle region is small, the SCC has not reached its yield limit, and the movement will be in a solid state.

3.2. Granular column collapse process

Through indoor experiments, Lacaze et al. (2008) investigated the influence of the initial aspect ratio on the collapse morphology of the particles in air, and they used the discrete element method (DEM) to reconstruct the granular collapse process. One group of experimental data and the DEM results of the process obtained by Zhang et al. (2021a) were used for comparison in this study. The particles initially accumulated on one side of a two-dimensional rectangular slot, with dimensions of 300 mm × 300 mm × 3 mm. The initial column width was 40 mm, and the height was 240 mm. A vertical gate was used to hold the column still. At the start of the experiment, the gate was pulled away instantaneously to allow the column to collapse freely. The particle density was 2650 kg/m^3, and the particles were approximately the same size, with a diameter of 2.5 mm. In this study, the internal friction angle was 30°. A 1:1 two-dimensional numerical model was created based on the experimental design. First, particles of approximately the same size were deposited on one side of the rectangular area. The remaining part of the area was air, and the ground of the area was a no-slip boundary. The left and right sides were free-slip boundaries with a pressure gradient of 0 Pa/m. The top velocity gradient was 0 (m/s)/m, and the pressure was 0 Pa. Fig. 5 shows the results of the column morphology at four moments, i.e., 0.15 s, 0.30 s, 0.45 s, and 0.60 s. The results of the Coulomb-viscoplastic model used in this study produced a slightly larger column height in the initial period compared with the experimental value. In the second half of the period, the column height was slightly lower than the experimental value. This may be due to the large internal friction angle of the particles. Fig. 6 shows the velocity map of the particles and air at different times (0.15 s, 0.30 s, 0.45 s, and 0.60 s), which divides the collapse process into several stages. Under the initial condition, the pressure at the bottom part (due to the weight of the mass above) is large, and the shear rate inside the particles is small. The apparent viscosity of the column at the bottom is large. Due to no block on the right, the upper and front part of the granular column move to the lower right (0.15 s). Then, the granular column changes to the B stage. Similarly, the apparent viscosity of the column at the bottom is large. The upper and front part of the column move to the lower right. Eventually, the column tends to the be static (D stage). In this study, we also present the results of the DEM simulation (Zhang et al., 2021a). The results show that the Coulomb-viscoplastic model was very close to the results of the DEM method. However, since the DEM method needs to simulate the collision between particles and track their positions, the corresponding calculation cost is large (Sundaresan et al., 2018; Li et al., 2020a). Although the results of the DEM are more accurate, it is unrealistic to apply it to three-dimensional numerical simulations of large-scale debris flows. In comparison, the proposed method balances the accuracy of the calculation and the amount of computation required and can be applied to the simulation of actual scale debris flows.

3.3. Debris flow simulation

The above two examples verified the effectiveness of the H–B–P model and the Coulomb-viscoplastic model. In this section, a three-phase flow example is used to verify the effectiveness of the *interDebrisFoam* solver. Hürlimann and Rickli (2015) studied the influence of soil water content, grain-size distribution and initial volume on the runout characteristics of hillslope debris flows based on laboratory

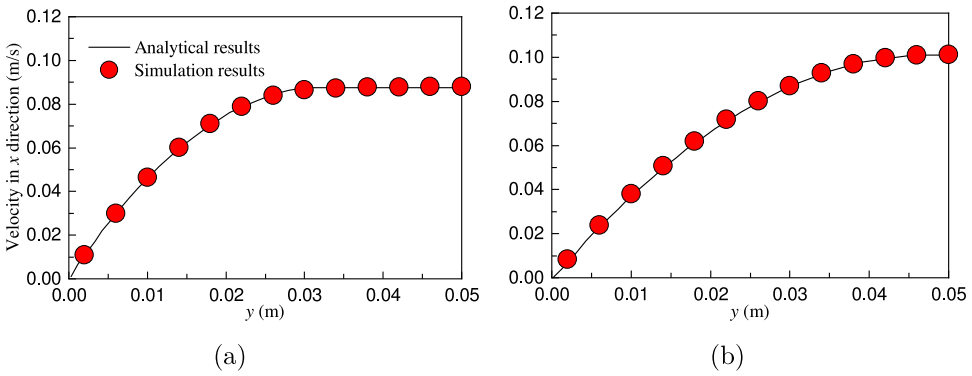

Fig. 4. Comparison between the numerical simulation results and the analytical solution: (a) SCC, and (b) Grout.

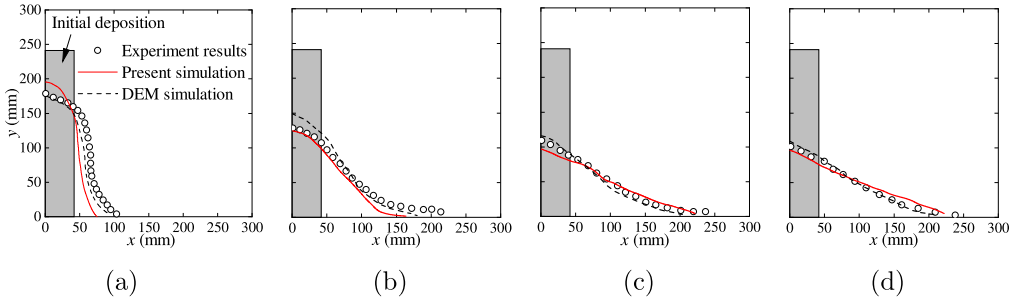

Fig. 5. Variation in the collapse height with time, (a) t = 0.15 s, (b) t = 0.30 s, (c) t = 0.45 s, and (d) t = 0.60 s. The grey box represents the initial state of the granular column.

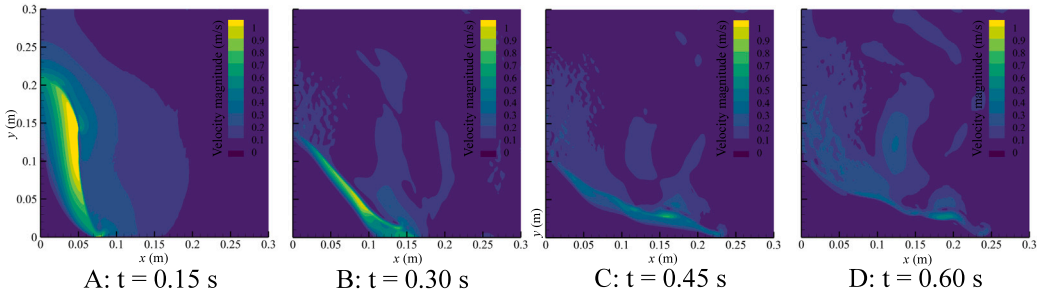

Fig. 6. The velocity map of the particles and air at different times (0.15 s, 0.30 s, 0.45 s, and 0.60 s).

experiments. The experimental hillslope is shown in Fig. 7, which consisted of four parts: (a) a 0.54 m long and 0.4 m wide head box, (b) a 4.46 m long and 1.2 m wide steep runout zone with an inclination of 30° (c) a 2.5 m long and 1.2 m wide lower-angle runout zone with a slope of 10° and (d) retention basin. Laser devices were used to determine the flow depth along the slope. The materials of the debris flow consisted of clay, silt, sand, gravel, and water. The water volume fraction is approximately 53%, and the clay fraction is approximately 7.5%. The initial volume of the debris flow mixture was 0.012 m^3, with the gravels accounting for 17%. The density of the slurry was set as 1400 kg/m^3. The density of the gravels was 2700 kg/m^3. The gravel friction angle was 36°. The free surface tension of the mixture and air was σ = 0.07 N/m. The constant $\mathbf{U}_r$ was set as −0.003 m/s in the vertical direction. The constant a was set as 0.5.

Fig. 8 shows the comparison between the simulated flow depth and the laser data (laser 1 and laser 2) in the experiment. The flow depth at the two laser locations presents a state of increasing first, then decreasing, and finally gradually stabilizing. This is because the flow head reaches the laser first with the maximum depth in the head. After the flow head moves downward, the rear part of the debris flow tends to be stable. However, the simulated flow depth is larger than the laser measurement data, which is evident at laser 2. In addition,

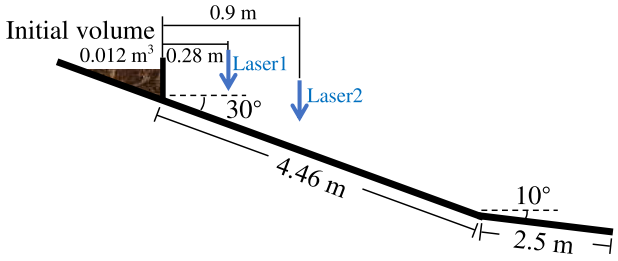

Fig. 7. Laboratory setup for the hillslope debris flow experiments. The two laser devices are used to determine the flow depth.

the simulated results are smoother than the measured data. This may result from the disturbance of the gravels in the laser measurement. Comparisons between laser data and the simulated results at such small scales are only approximate due to the surface disturbance by the gravels. The arrival time, the maximum depth, and the depth trend are more suitable for comparison. From this point of view, the model in this paper can reproduce the movement characteristics of debris flows.

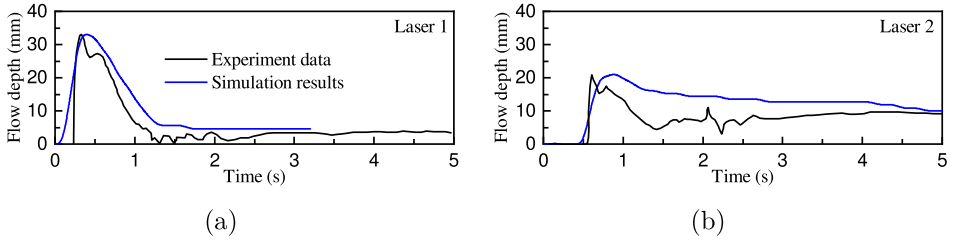

Fig. 8. Simulated flow depth and the laser measurement flow depth over time.

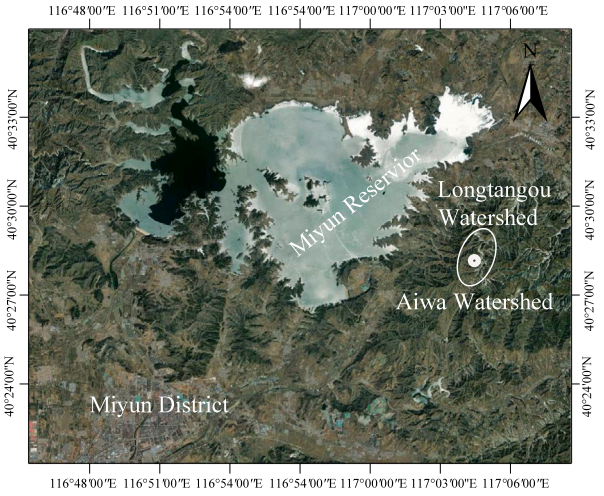

Fig. 9. Location of Miyun district.

4. Application to predicting the debris flow in the Longtangou Watershed

In 2011 and 2012, heavy rainfall triggered debris flows in the Pinggu and Miyun Districts of Beijing, damaging multiple bridges, causing direct economic losses of tens of billions of Yuan, and displacing nearly 6000 people (Li et al., 2019a). The Miyun District is located in the northeastern part of Beijing (Fig. 9). It is one of the high-risk areas for debris flows in the mountainous area of Beijing. In 1989, 1991, 2011, 2013, and 2016, severe mountain torrents and debris flows occurred in this area (Ma et al., 2016, 2018). The Longtangou Watershed is located in Taishitun Town in the northeastern part of the Miyun District, and it is a transition zone between the mountains and plains. In the Longtangou Watershed area, the mountains are steep, with an average slope of 42.1°. The terrain is undulating; it is high in the southern and central parts and low in the northwest. The highest elevation is 903 m, and the lowest is 255 m, with an elevation difference of 648 m. Due to the steep terrain, there is an obvious development of fractures and folds, as well as outcrops of ancient strata. Mountain torrents and debris flows occurred in the Longtangou Watershed in 2011, 2013, and 2016. Since the area is located to the east of the Miyun Reservoir, debris flows can threaten the safety of the cities and towns downstream and the water quality of the Miyun Reservoir. Preliminary remote sensing image data reveal that since 2012, the areas of the material source bodies in two ditch channels have increased rapidly, and it would be very easy for mountain torrents and debris flows to occur again. In this paper, based on the proposed numerical model, we explored the dynamic characteristics of the debris flow in the Longtangou Watershed in an attempt to provide a reference for the safe management of downstream towns and reservoirs.

The Longtangou Watershed contains several branches, among which the Aiwa Watershed has experienced the most severe debris flows (Zhang et al., 2018). The debris flows in the Aiwa Watershed pose great threats to the downstream roads (Fig. 10). The debris flows in 2011 and 2016 caused traffic disruptions. The valley of the watershed is shaped like a gravel leaf, and the watershed area is less than 1 km^2. The smaller area significantly increases the possibility of debris flows (Table 2). The elevation difference of the ditch is 0.44 km, and the drop in the ditch bed profile is larger than 30%. The Aiwa Watershed has a wide variety of material sources. The main materials include collapse deposits, channel slope deposits, channel bed deposits, and old debris flow deposits. Among them, collapse deposits are the main material source in the Aiwa Watershed (50%), and the diameter of the collapse deposits is 30?0 mm. The structure is complex, with large pores and low stability. Remote sensing images show that the area of the material sources in the Aiwa Watershed has increased from 1674 m^2 in 2012 to 20284 m^2 in 2016 (Zhang et al., 2018). Currently, the material source is rich in this area, providing the necessary conditions for the occurrence of more debris flows.

Zhang et al. (2018) sampled the deposits in the Aiwa Watershed and analysed their density and composition. During sampling, the top 10 cm on the surface of the deposits was removed first, and the underlying debris flow deposit in the lower part was collected. The samples were screened using a 60 mm steel sieve to remove the large gravel. Samples with a particle size of less than 60 mm were included in this study. The samples were sealed and brought back to the laboratory to measure their weights and volumes. It was calculated that the densities of the large debris flow and solid samples (> 20 mm) were 1900 kg/m^3 and 2500 kg/m^3, respectively, the clay fraction was 5%, and the water content was 15%–30%. In this study, the water content was taken as 22.5%. The volume fraction of the gravels in the sample is approximately 0.17. The constant $\mathbf{U}_r$ was set as −0.5 m/s in the vertical direction. The constant a was set as 0.5.

4.1. Numerical setup

In the numerical simulation of a debris flow, one of the most important factors is to determine the terrain of the debris flow area in the computational domain. The terrain has a significant influence on the debris flow velocity, runout path, and distance due to the variations in the gradient of the terrain. The fine terrain, which is closer to the real landform, has more obvious topographic fluctuations than the coarse terrain, making the numerical simulation results more in line with a realistic debris flow. Another key factor is the initial volume of the debris flow, which also directly affects the flow characteristics of the debris flow, such as the runout distance, the affected area, the velocity, and the depth of the deposit. Thus, a reasonable initial debris flow volume estimation is essential.

The topographic boundaries of the Aiwa Watershed were constructed using a digital elevation model. According to the location of the Aiwa Watershed in Fig. 10(a), the elevation data were obtained from the public digital elevation model data, which were then imported into ANSYS SCDM to generate the calculation domain. The domain was meshed in FLUENT Meshing, and then OpenFOAM was used for the numerical simulation. Fig. 11(b) shows the meshed Aiwa watershed area shown in Fig. 10(a). In total, the mesh contains approximately 6 million cells when the mesh size is 2 m in all directions. The ground of

Table 2
Topographic parameters of the Aiwa Watershed.

Basin area (km^2)	Channel length (km)	Relative elevation (km)	Longitudinal gradient (%)	Slope gradient (°)
0.34	1.13	0.44	32.3	23.5

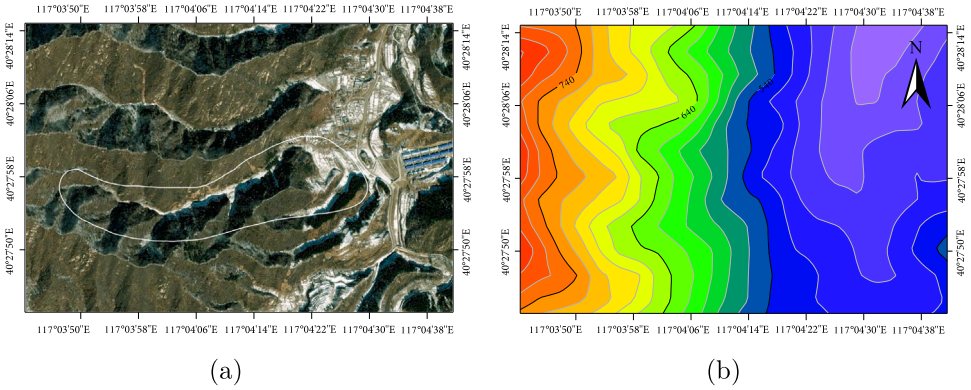

Fig. 10. (a) Location of the Aiwa Watershed and (b) elevation map of the Aiwa Watershed.

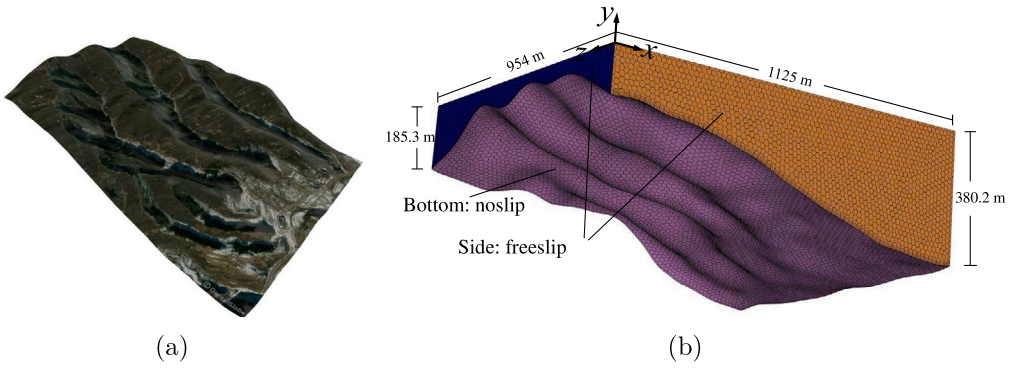

Fig. 11. (a) Topographic map of the Aiwa Watershed and (b) meshing of the Aiwa Watershed calculation domain.

the calculation domain is the 1:1 terrain surface of the Aiwa Watershed, and a no-slip boundary condition was used; the velocity was 0 m/s, and the pressure gradient was 0 Pa/m. The four sides were free-slip boundaries. The pressure gradient was also 0 Pa/m, the ground pressure was 0 Pa, and the velocity gradient was 0 (m/s)/m. Furthermore, the travel distance and extent of a debris flow are affected by the rheological properties of the slurry and gravel. According to the discussion in the previous section, the density of the slurry was set to 1900 kg/m^3, and the density of the gravel was set to 2500 kg/m^3. The yield stress of the slurry was obtained from Eq. (40), $\tau = 26.58$ Pa, flow index $n = 1$, consistency index $k = 8.86$ Pa·s, stress growth parameter $m = 5$ s, internal friction angle of gravels $\theta = 30°$, $s = 1.0$ s. According to the geological survey of Tu (2017), the volume of sediment supplements in the Aiwa Watershed is approximately 143300 m^3. Hence, a certain amount (approximately 0.14 km^3) of debris flow was set at the top of the slope, the volume fraction of the slurry was 0.83, the volume fraction of the gravel was 0.17, and the remaining part was air, with a volume fraction of 1. Finally, the associated fields were decomposed into multiple blocks using the decomposePar tool, and each separate block in the decomposed fields was run on the cluster of the BeiJing High Performance Computing (HPC) with 64 AMD EPYC 7452 CPU 2.35 GHz and 256 GB RAM using OpenMPI (an implementation of the standard message passing interface). The simulation calculation was conducted based on OpenFOAM with a computation time of approximately 12.5 h.

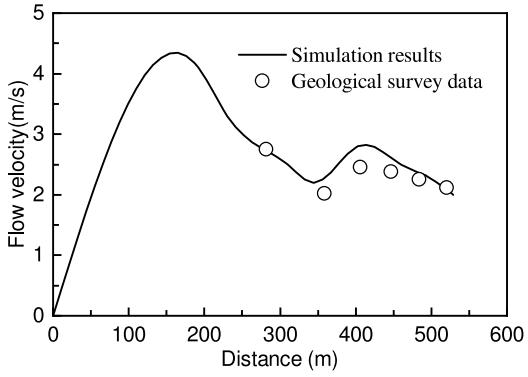

Fig. 12. Comparison between the simulation results and the geological survey data of the flow velocity. The distance indicates the difference between the x-coordinates of debris front.

4.2. Results and discussion

First, we verify the optimized model in the field case. The debris flow in 2016 in the Aiwa Watershed is simulated. The initial volume of the debris flow is approximately 38540 m^3 (Zhang et al., 2018). The debris flow velocity at different places of the Aiwa Watershed was obtained based on a geological survey method. Fig. 12 shows the comparison between the simulation results and the geological survey

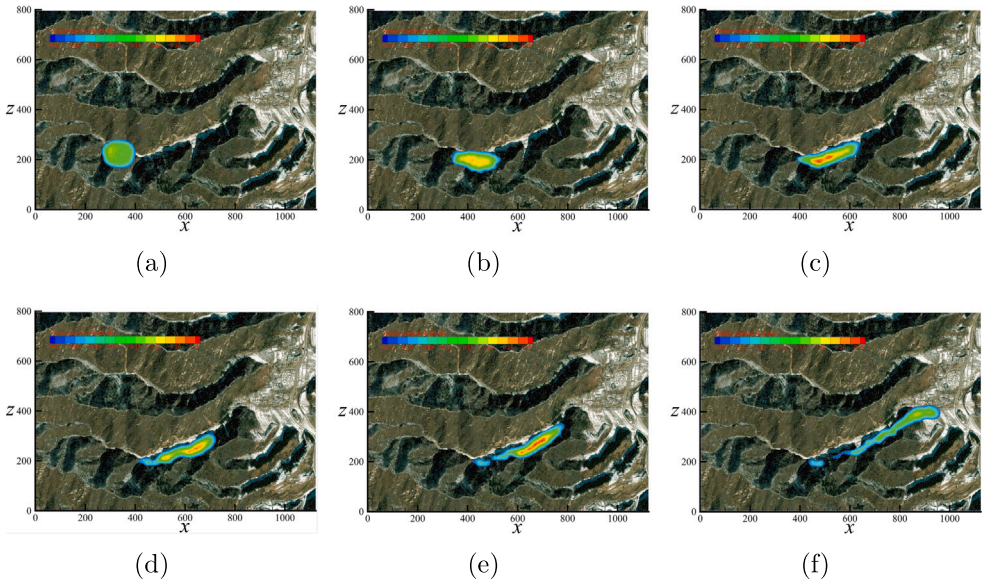

Fig. 13. The evolution of the volume fraction of the gravels with space and time for (a) t = 0 s, (b) t = 20 s, (c) t = 40 s, (d) t = 60 s, (e) t = 80 s, and (f) t = 120 s. The base map is a satellite image.

data. The simulation result is close to the geological survey result, and the trend of the flow velocity is the same as the geological survey result.

Then, the optimized method was used to simulate the movement and accumulation of the debris flow, which may occur in the future. The Aiwa Watershed's ditch is approximately C-shaped, and there is a topographic transition at approximately x = 400 m. We analysed the movement of the Aiwa Watershed debris flow at 10 s intervals. Fig. 13 gives the evolution of the volume fraction of the gravels with space and time. The simulation results based on the method proposed by von Boetticher et al. (2016) are also shown in Fig. 14. At the beginning, the slurry and the gravels are uniformly mixed. After it began to move down the slope, the gravels settled to the bottom of the mixture due to the density difference between the slurry and the gravels. The gravels moves faster than the slurry. As a result, the gravels go to the flow front, making the volume fraction of the gravels at the front of the debris flow larger than 0.17 (with a maximum value of approximately 0.3). However, the volume fraction of the gravels from the method of von Boetticher et al. (2016) shows uniform distribution characteristics over time (Fig. 14). This is because the method of von Boetticher et al. (2016) does not consider the interaction between slurry and gravels. The two phases have the same velocity and pressure in each calculating cell. However, the method in the present paper considers the velocity slip (or two-phase interaction) between the slurry and the gravels. The gravels and slurry have different moving velocities around space and time. In addition, comparing Figs. 13(e) and 14(c), the running distance in the present simulation at 80 s is the same as the method of von Boetticher et al. (2016) at 100 s. This means that the flow velocity obtained based on the method of this work is larger than the method proposed by von Boetticher et al. (2016), which results from the gravels moving to the flow front. More gravel at the flow front will increase the flow velocity. In addition, an important difference between the two simulation results is the distribution form of the debris flow. More debris flows are distributed at the front in this paper, while in the method of von Boetticher et al. (2016), the entire debris flow is evenly distributed and presents an approximate rectangle.

Fig. 15 shows the velocity and morphology of the debris flow at different moments (t = 10 s, 30 s, and 100 s). The movement boundary of the debris flow was determined by the free surface (isosurface of α_a = 0.5). Fig. 16 gives the change in the volumetric velocity of the front edge of the free surface with time. Once the debris flow started to move, the gravitational potential energy of the debris flow was converted into kinetic energy, causing the velocity to increase gradually, with a maximum velocity magnitude of approximately 10 m/s. The maximum velocity of the debris flow occurred near its front edge. Subsequently, it took approximately 10 s for the debris flow to travel approximately 200 m and reach the bend (point A in Fig. 16) in the Aiwa Watershed, with a velocity of approximately 10 m/s. The flow velocity significantly decreases due to bend hindrance. Once a large-scale debris flow is formed, it will cause strong erosion of the banks on both sides of the bend and wash away the material sources in the foot area. Moreover, landslides easily occur on the erosion bank, blocking the channel and forming a blocking-collapse debris flow, which will increase the severity and scale of the debris flow. The accumulation area is relatively flat and open, and the pressure of the debris flow on the bed is small. Since there are residential areas and roads along the Aiwa Watershed, the occurrence of debris flows seriously threatens the lives and property of local residents. Therefore, proper measures should be taken to prevent large-scale debris flows from causing damage.

Subsequently, the debris flow flowed through a 500 m linear section. The velocity of the debris flow increases slightly under the action of gravity due to the straightening of the slope (point B in Fig. 16). However, due to the decrease in the slope and the friction of the channel, the velocity of the debris flow decreases near the smoother mouth area of the ditch, and the debris flow gradually accumulates in this area. Moreover, as the velocity decreases, the internal shear rate decreases, and the viscosity of the slurry and gravels increases rapidly, which further reduces the velocity of the debris flow (points C to D in Fig. 16). At point D (Fig. 16), there is a steep drop. Hence, the flow velocity increases slightly. Finally, at approximately 120 s (point E in Fig. 16), it flowed into villages and onto the roads in the eastern part of the Aiwa Watershed, with an average velocity of approximately 4 m/s, and the total travel distance was approximately 800 m. Such a velocity would cause huge damage to the buildings and roads in this area and could even result in casualties. Furthermore, due to geographic factors, the flow velocity of the debris flow rapidly decreased. In conclusion, the simulation results show that a debris flow in the Aiwa Watershed could severely impact the downstream area. Thus, preventative measures are needed.

Limited by the topography of the Aiwa Watershed, the debris flow mainly flowed along the Aiwa Watershed channel. To study the sectional morphological changes in the debris flow, a height map of the debris flow at different moments (t = 40 s, 80 s, and 120 s) is shown in Fig. 17. The thickness of the debris flow is directly related to the

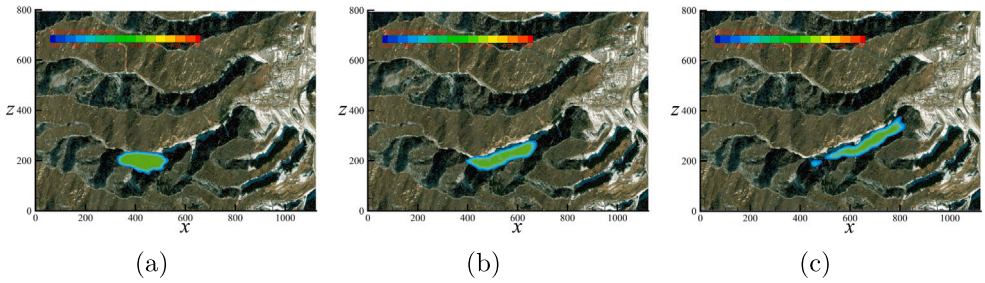

Fig. 14. The evolution of the volume fraction of the gravels with space and time for (a) $t = 10$ s, (b) $t = 50$ s, and (c) $t = 100$ s based on the method proposed by von Boetticher et al. (2016). The base map is a satellite image.

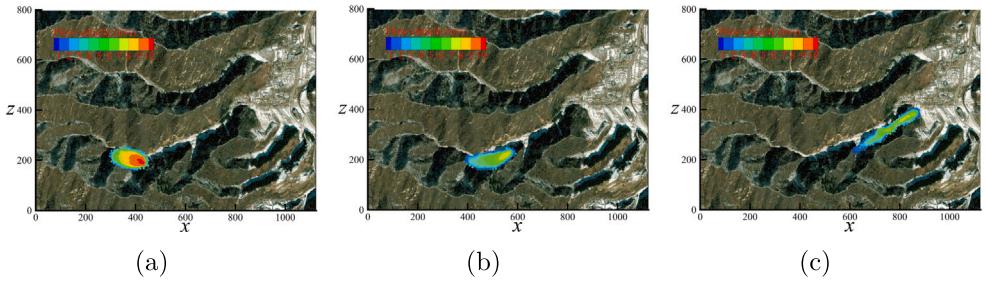

Fig. 15. The time sequence of the numerical simulation results of the debris flow in the Aiwa Watershed for (a) 10 s, (b) 30 s, and (c) 100 s. The base map is a satellite image. The colour map of the simulation results was mapped using the free surface and the magnitude of the velocity.

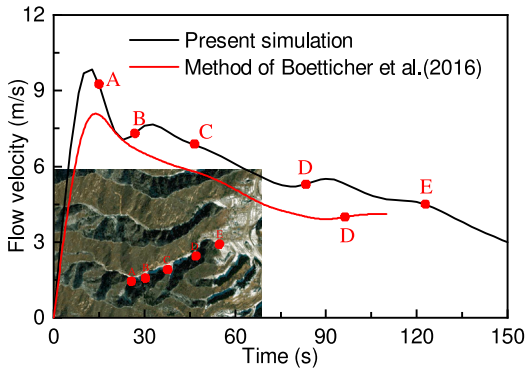

Fig. 16. Change in the volumetric velocity of the front edge of the free surface of the debris flow with time.

topography of the channel. The highest section was located at the front part of the debris flow, and the height in the second half of the channel remained the same. This is because this part of the Aiwa Watershed is straight, and the depth is fairly uniform. Thus, the debris flow reached a stable state in this part of the channel. When the debris flow reached the bottom, the debris flow expanded into a fan shape, and it gradually accumulated in this area, causing the height of the debris flow to increase. From the numerical simulation results of the debris flow in the Aiwa Watershed, it can reasonably be concluded that the proposed method can be used to represent the entire movement pattern of a debris flow on actual terrain.

Finally, to improve the appreciation of the present model's free parameters, the effects of two factors (the initial volume fraction of the gravels and water content) on the predicted flow dynamics of the debris flow are given. The initial volume fraction of the gravels is set as 0.6, 0.4, and 0.17. The water content of the slurry is set as 20% (τ_0 = 58.7 Pa, k = 19.4 Pa), 22.5% (τ_0 = 26.6 Pa, k = 8.9 Pa), and 25% (τ_0 = 15.9 Pa, k = 5.3 Pa), respectively. All other parameters are the same as the former setting in the debris flow in the Aiwa Watershed. Fig. 18 shows the flow velocity with time at different initial volume fractions of the gravels and water contents. The flow velocity increases significantly with the increase in the initial volume fraction of the gravels and the water content. More gravels cause the density of the mixture to increase, and the acceleration of downward movement is also greater. In addition, more gravels moving to the front of the debris flow will further increase the velocity. When the water content increases, the yield strength of the slurry decreases, and the fluidity of the debris flow becomes stronger, resulting in an increase in the movement velocity.

5. Conclusions

Debris flow can potentially cause great damage to buildings and people downstream, and thus, it is of great significance to study the movement characteristics and development trends of debris flows. The topic of debris flow disaster prevention has been discussed extensively in government departments. The movement characteristics of debris flows are complex and are affected by various factors, such as the composition, water content, slope and roughness of the terrain, and material sources. In this study, we developed a numerical method to simulate the 3D movement and development of a real debris flow. The Navier–Stokes equations, the H–B–P model, and the pressure-dependent Coulomb viscoplastic model were introduced into the OpenFOAM framework, a free, open-source, parallel processing software backed by a large user-driven support community. To verify the performance of the method, the numerical method was tested in some cases. The flow between two parallel plates was used to verify the H–B–P model implanted in OpenFOAM, and a granular column collapse experiment was conducted to verify the pressure-dependent Coulomb viscoplastic model. In addition, a three-phase debris flow experiment was used to verify the effectiveness of the interDebrisFoam solver.

This method was also used to predict the route and impact area of a debris flow across the Aiwa Watershed. To construct a wide range of detailed downstream terrain in the Aiwa Watershed, digital elevation model data were used to sample the surface information. In addition, a parallel technique was applied to simulate the complex problem and attain reasonable debris flow predictions. The results show that a debris flow in the Aiwa Watershed would flow at a maximum speed of 10 m/s

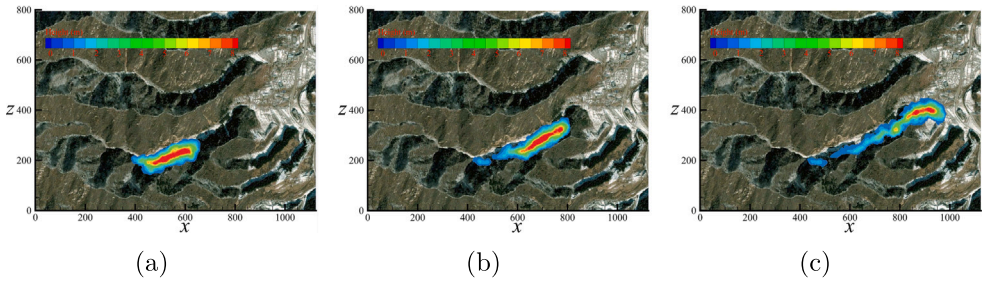

Fig. 17. Change in the height of the debris flow in the Aiwa Watershed with time: (a) $t = 40$ s, (b) $t = 80$ s, and (c) $t = 120$ s. The base map is the satellite image. The colour map of the simulation results was mapped using the free surface and the debris height.

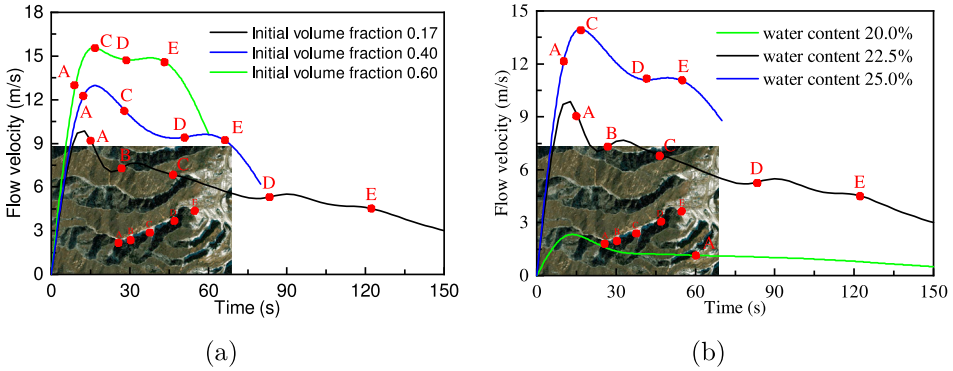

Fig. 18. Flow velocity of the debris flow with time at different (a) initial volume fractions of the gravels and (b) water contents.

and could cause severe damage to the villages and roads downstream. Thus, preventative measures are needed. In conclusion, the proposed numerical method is an effective approach for modelling debris flows, estimating hazard intensity, and designing protective measures.

CRediT authorship contribution statement

Yan Zhang: Methodology, Software, Validation, Data curation, Writing – original draft. **Liqun Lyu:** Validation, Investigation, Writing – review & editing, Funding acquisition, Supervision. **Peng Li:** Funding acquisition, Writing – review & editing.

Declaration of competing interest

The authors declare that they have no known competing financial interests or personal relationships that could have appeared to influence the work reported in this paper.

Data availability statement

The source code can be downloaded from https://github.com/YanZhang-cas/interDebrisFoam.git. Please follow the instructions given in the README.pdf file for installation of the *interDebrisFoam*.

Acknowledgements

We gratefully acknowledge the Beijing Municipal Education Commission, China for their financial support through the Innovative Transdisciplinary Programme "Ecological Restoration Engineering".

References

Adebiyi, A.A., Hu, P., 2021. A numerical study on impacts of sediment erosion/deposition on debris flow propagation. Water 13 (1698), http://dx.doi.org/10.3390/w13121698.

Albadawi, A., Donoghue, D., Robinson, A., Murray, D., Delauré, Y., 2013. Influence of surface tension implementation in volume of fluid and coupled volume of fluid with level set methods for bubble growth and detachment. Int. J. Multiph. Flow. 53, 11–28. http://dx.doi.org/10.1016/j.ijmultiphaseflow.2013.01.005.

Allstadt, K.E., Matoza, R.S., Lockhart, A.B., Moran, S.C., Caplan-Auerbach, J., Haney, M.M., Thelen, W.A., Malone, S.D., 2018. Seismic and acoustic signatures of surficial mass movements at volcanoes. J. Volcanol. Geotherm. Res. 364, 76–106. http://dx.doi.org/10.1016/j.jvolgeores.2018.09.007.

Benn, D.I., Bolch, T., Hands, K., Gulley, J., Luckman, A., Nicholson, L.I., Quincey, D., Thompson, S., Toumi, R., Wiseman, S., 2012. Response of debris-covered glaciers in the mount everest region to recent warming, and implications for outburst flood hazards. Earth-Sci. Rev. 114, 156–174. http://dx.doi.org/10.1016/j.earscirev.2012.03.008.

Berberović, E., van Hinsberg, N.P., Jakirlić, S., Roisman, I.V., Tropea, C., 2009. Drop impact onto a liquid layer of finite thickness: Dynamics of the cavity evolution. Phys. Rev. E 79, 036306. http://dx.doi.org/10.1103/PhysRevE.79.036306.

von Boetticher, A., Turowski, J.M., McArdell, B.W., Rickenmann, D., Kirchner, J.W., 2016. Debrisintermixing-2.3: A finite volume solver for three-dimensional debris-flow simulations with two calibration parameters – Part 1: Model description. Geosci. Model Dev. 9, 2909–2923. http://dx.doi.org/10.5194/gmd-10-3963-2017.

Bohorquez, P., 2012. Finite volume method for falling liquid films carrying monodisperse spheres in newtonian regime. AIChE J. 58, 2601–2616. http://dx.doi.org/10.1002/aic.13863.

Coussot, P., Laigle, D., Arattano, M., Deganutti, A., Marchi, L., 1998. Direct determination of rheological characteristics of debris flow. J. Hydraul. Eng. 124, 865–868. http://dx.doi.org/10.1061/(ASCE)0733-9429(1998)124:8(865).

Dai, Z., Huang, Y., Cheng, H., Xu, Q., 2014. 3D numerical modeling using smoothed particle hydrodynamics of flow-like landslide propagation triggered by the 2008 Wenchuan earthquake. Eng. Geol. 180, 21–33. http://dx.doi.org/10.1016/j.enggeo.2014.03.018.

Damián, S.M., Nigro, N.M., 2014. An extended mixture model for the simultaneous treatment of small-scale and large-scale interfaces. Internat. J. Numer. Methods Fluids 75, 547–574. http://dx.doi.org/10.1002/fld.3906.

Deshpande, S.S., Anumolu, L., Trujillo, M.F., 2012. Evaluating the performance of the two-phase flow solver interfoam. Comput. Sci. Discov. 5, 014016. http://dx.doi.org/10.1088/1749-4699/5/1/014016.

Domnik, B., Pudasaini, S.P., 2012. Full two-dimensional rapid chute flows of simple viscoplastic granular materials with a pressure-dependent dynamic slip-velocity and their numerical simulations. J. Non-Newton. Fluid Mech. 173-174, 72–86. http://dx.doi.org/10.1016/j.jnnfm.2012.03.001.

Domnik, B., Pudasaini, S.P., Katzenbach, R., Miller, S.A., 2013. Coupling of full two-dimensional and depth-averaged models for granular flows. J. Non-Newton. Fluid Mech. 201, 56–68. http://dx.doi.org/10.1016/j.jnnfm.2013.07.005.

Duy, T.N., Nguyen, V.T., Phan, T.H., Park, W.G., 2021. An enhancement of coupling method for interface computations in incompressible two-phase flows. Comput. & Fluids 214, 104763. http://dx.doi.org/10.1016/j.compfluid.2020.104763.

Fang, J., Wang, L., Hong, Y., Zhao, J., 2021. Influence of solid–fluid interaction on impact dynamics against rigid barrier: CFD–DEM modelling. Géotechnique 1–16. http://dx.doi.org/10.1680/jgeot.19.P.160.

Forterre, Y., Pouliquen, O., 2008. Flows of dense granular media. Annu. Rev. Fluid Mech. 40, 1–24. http://dx.doi.org/10.1146/annurev.fluid.40.111406.102142.

Friedemann, C., Mortensen, M., Nossen, J., 2021. Two-phase co-current flow simulations using periodic boundary conditions in horizontal, 4, 10 and 90° inclined eccentric annulus, flow prediction using a modified interfoam solver and comparison with experimental results. Int. J. Heat Fluid Flow 88, 108754. http://dx.doi.org/10.1016/j.ijheatfluidflow.2020.108754.

Goodwin, G., Choi, C., 2020. Slit structures: Fundamental mechanisms of mechanical trapping of granular flows. Comput. Geotech. 119, 103376. http://dx.doi.org/10.1016/j.compgeo.2019.103376.

Gopala, V.R., Lycklama à Nijeholt, J.A., Bakker, P., Haverkate, B., 2011. Development and validation of a CFD model predicting the backfill process of a nuclear waste gallery. Nucl. Eng. Des. 241, 2508–2518. http://dx.doi.org/10.1016/j.nucengdes.2011.04.021.

sen Guo, X., feng Zheng, D., kai Nian, T., Yin, P., 2019. Effect of different span heights on the pipeline impact forces induced by deep-sea landslides. Appl. Ocean Res. 87, 38–46. http://dx.doi.org/10.1016/j.apor.2019.03.009.

Guzzetti, F., Peruccacci, S., Rossi, M., Stark, C.P., 2008. The rainfall intensity-duration control of shallow landslides and debris flows: An update. Landslides 5, 3–17. http://dx.doi.org/10.1007/s10346-007-0112-1.

Han, Z., Chen, G., Li, Y., Tang, C., Xu, L., He, Y., Huang, X., Wang, W., 2015a. Numerical simulation of debris-flow behavior incorporating a dynamic method for estimating the entrainment. Eng. Geol. 190, 52–64. http://dx.doi.org/10.1016/j.enggeo.2015.02.009.

Han, Z., Chen, G., Li, Y., Wang, W., Zhang, H., 2015b. Exploring the velocity distribution of debris flows: An iteration algorithm based approach for complex cross-sections. Geomorphology 241, 72–82. http://dx.doi.org/10.1016/j.geomorph.2015.03.043.

Han, Z., Su, B., Li, Y., Wang, W., Wang, W., Huang, J., Chen, G., 2019. Numerical simulation of debris-flow behavior based on the SPH method incorporating the Herschel-Bulkley-Papanastasiou rheology model. Eng. Geol. 255, 26–36. http://dx.doi.org/10.1016/j.enggeo.2019.04.013.

Hirt, C., Nichols, B., 1981. Volume of fluid (VOF) method for the dynamics of free boundaries. J. Comput. Phys. 39, 201–225. http://dx.doi.org/10.1016/0021-9991(81)90145-5.

Huang, X., García, M.H., 1997. A perturbation solution for bingham-plastic mudflows. J. Hydraul. Eng. 123, 986–994. http://dx.doi.org/10.1061/(ASCE)0733-9429(1997)123:11(986).

Huang, Y., Zhang, W., Xu, Q., Xie, P., Hao, L., 2012. Run-out analysis of flow-like landslides triggered by the ms 8.0 2008 Wenchuan earthquake using smoothed particle hydrodynamics. Landslides 9, 275–283. http://dx.doi.org/10.1007/s10346-011-0285-5.

Hürlimann, B.W., Rickli, C., 2015. Field and laboratory analysis of the runout characteristics of hillslope debris flows in Switzerland. Geomorphology 232, 20–32. http://dx.doi.org/10.1016/j.geomorph.2014.11.030.

Imran, J., Parker, G., Locat, J., Lee, H., 2001. 1D numerical model of muddy subaqueous and subaerial debris flows. J. Hydraul. Eng. 127, 959–968. http://dx.doi.org/10.1061/(ASCE)0733-9429(2001)127:11(959).

Issa, R., Gosman, A., Watkins, A., 1986. The computation of compressible and incompressible recirculating flows by a non-iterative implicit scheme. J. Comput. Phys. 62, 66–82. http://dx.doi.org/10.1016/0021-9991(86)90100-2.

Jasak, H., 1996. Error Analysis and Estimation for the Finite Volume Method with Applications to Fluid Flows (Ph.D. thesis). Imperial College London, University of London.

Jasak, H., Jemcov, A., Tukovic, Z., et al., 2007. Openfoam: A c++ library for complex physics simulations. In: International Workshop on Coupled Methods in Numerical Dynamics. IUC Dubrovnik Croatia, pp. 1–20.

Jeong, S., Lee, K., 2019. Analysis of the impact force of debris flows on a check dam by using a coupled Eulerian-Lagrangian (CEL) method. Comput. Geotech. 116, 103214. http://dx.doi.org/10.1016/j.compgeo.2019.103214.

Jop, P., Forterre, Y., Pouliquen, O., 2006. A constitutive law for dense granular flows. Nature 441, 727–730. http://dx.doi.org/10.1038/nature04801.

Kang, H.S., Kim, Y.T., 2017. Rheological properties of loose sands subjected to upward flow. Can. Geotech. J. 54, 664–673. http://dx.doi.org/10.1139/cgj-2016-0171.

Kong, Y., Zhao, J., Li, X., 2021. Hydrodynamic dead zone in multiphase geophysical flows impacting a rigid obstacle. Powder Technol. 386, 335–349. http://dx.doi.org/10.1016/j.powtec.2021.03.053.

Lacaze, L., Phillips, J.C., Kerswell, R.R., 2008. Planar collapse of a granular column: Experiments and discrete element simulations. Phys. Fluids 20, 063302. http://dx.doi.org/10.1063/1.2929375.

Lee, K., Kim, Y., Ko, J., Jeong, S., 2019. A study on the debris flow-induced impact force on check dam with- and without-entrainment. Comput. Geotech. 113, 103104. http://dx.doi.org/10.1016/j.compgeo.2019.103104.

Li, J., Cao, Z., Pender, G., Liu, Q., 2013. A double layer-averaged model for dam-break flows over mobile bed. J. Hydraul. Res. 51, 518–534. http://dx.doi.org/10.1080/00221686.2013.812047.

Li, Y., Ma, C., Wang, Y., 2019a. Landslides and debris flows caused by an extreme rainstorm on 21 july 2012 in mountains near Beijing, China. Bull. Eng. Geol. Environ. 78, 1265–1280. http://dx.doi.org/10.1007/s10064-017-1187-0.

Li, D., Marchisio, D., Hasse, C., Lucas, D., 2020a. twoWayGPBEFoam: An open-source Eulerian QBMM solver for monokinetic bubbly flows. Comput. Phys. Comm. 250, 107036. http://dx.doi.org/10.1016/j.cpc.2019.107036.

Li, P., Zhang, X., Lu, X., 2019b. Three-dimensional Eulerian modeling of gas–liquid–solid flow with gas hydrate dissociation in a vertical pipe. Chem. Eng. Sci. 196, 145–165. http://dx.doi.org/10.1016/j.ces.2018.10.053.

Li, X., Zhao, J., 2018. A unified CFD-DEM approach for modeling of debris flow impacts on flexible barriers. Int. J. Numer. Anal. Methods Geomech. 42, 1643–1670. http://dx.doi.org/10.1002/nag.2806.

Li, X., Zhao, J., Kwan, J.S., 2020b. Assessing debris flow impact on flexible ring net barrier: A coupled CFD-DEM study. Comput. Geotech. 128, 103850. http://dx.doi.org/10.1016/j.compgeo.2020.103850.

Liang, Q., Xia, X., Hou, J., 2015. Efficient urban flood simulation using a gpu-accelerated SPH model. Environ. Earth Sci. 74, 7285–7294. http://dx.doi.org/10.1007/s12665-015-4753-4.

Lu, P.y., Yang, X.g., Xu, F.g., Hou, T.x., Zhou, J.w., 2016. An analysis of the entrainment effect of dry debris avalanches on loose bed materials. SpringerPlus 5, 1–15. http://dx.doi.org/10.1186/s40064-016-3272-4.

Ma, C., Deng, J., Wang, R., 2018. Analysis of the triggering conditions and erosion of a runoff-triggered debris flow in miyun county, Beijing, China. Landslides 15, 2475–2485. http://dx.doi.org/10.1007/s10346-018-1080-3.

Ma, C., Wang, Y.jie., Du, C., Wang, Y.qi., Li, Y.peng., 2016. Variation in initiation condition of debris flows in the mountain regions surrounding Beijing. Geomorphology 273, 323–334. http://dx.doi.org/10.1016/j.geomorph.2016.08.027.

Nguyen, V., Kang, H.S., Kim, Y.T., 2018. Effect of clay fraction and water content on rheological properties of sand–clay mixtures. Environ. Earth Sci. 77, 576. http://dx.doi.org/10.1007/s12665-018-7748-0.

Nguyen Duy, T., Hino, T., 2020. An improvement of interface computation of incompressible two-phase flows based on coupling volume of fluid with level-set methods. Int. J. Comput. Fluid Dyn. 34, 75–89. http://dx.doi.org/10.1080/10618562.2020.1720000.

Pang, B., Wang, S., Liu, G., Jiang, X., Lu, H., Li, Z., 2018. Numerical prediction of flow behavior of cuttings carried by Herschel-Bulkley fluids in horizontal well using kinetic theory of granular flow. Powder Technol. 329, 386–398. http://dx.doi.org/10.1016/j.powtec.2018.01.065.

Papanastasiou, T., 1987. Flow material with yield. J. Rheol. 31, 385–404. http://dx.doi.org/10.1122/1.549926.

Pastor, M., Blanc, T., Haddad Akni, B., Petrone, S., Sanchez, M., Drempetic, V., Issler, D., Crosta, G., Cascini, L., Sorbino, G., Cuomo, S., 2014. Application of a SPH depth-integrated model to landslide run-out analysis. Landslides 11, 793–812. http://dx.doi.org/10.1007/s10346-014-0484-y.

Qian, X., Das, H.S., 2019. Modeling subaqueous and subaerial muddy debris flows. J. Hydraul. Eng. 145, 04018083. http://dx.doi.org/10.1061/(ASCE)HY.1943-7900.0001526.

Rhie, C.M., Chow, W.L., 1983. Numerical study of the turbulent flow past an airfoil with trailing edge separation. AIAA J. 21, 1525–1532. http://dx.doi.org/10.2514/3.8284.

Shen, W., Li, T., Li, P., Lei, Y., 2020. Numerical assessment for the efficiencies of check dams in debris flow gullies: A case study. Comput. Geotech. 122, 103541. http://dx.doi.org/10.1016/j.compgeo.2020.103541.

Song, D., Ng, C., Choi, C., Zhou, G., Kwan, J., Koo, R., 2017. Influence of debris flow solid fraction on rigid barrier impact. Can. Geotech. J. 54, 1421–1434. http://dx.doi.org/10.1139/cgj-2016-0502.

Song, D., Zhou, G.G., Chen, X.Q., Li, J., Wang, A., Peng, P., Xue, K.X., 2021. General equations for landslide-debris impact and their application to debris-flow flexible barrier. Eng. Geol. 288, 106154. http://dx.doi.org/10.1016/j.enggeo.2021.106154.

Sundaresan, S., Ozel, A., Kolehmainen, J., 2018. Toward constitutive models for momentum, species, and energy transport in gas–particle flows. Annu. Rev. Chem. Biomol. Eng. 9, 61–81. http://dx.doi.org/10.1146/annurev-chembioeng-060817-084025.

Takebayashi, H., Fujita, M., 2020. Numerical simulation of a debris flow on the basis of a two-dimensional continuum body model. Geosciences 10 (45), http://dx.doi.org/10.3390/geosciences10020045.

Tayyebi, S.M., Pastor, M., Stickle, M.M., 2021. Two-phase sph numerical study of pore-water pressure effect on debris flows mobility: Yu tung debris flow. Comput. Geotech. 132, 103973. http://dx.doi.org/10.1016/j.compgeo.2020.103973.

Toniolo, H., Harff, P., Marr, J., Paola, C., Parker, G., 2004. Experiments on reworking by successive unconfined subaqueous and subaerial muddy debris flows. J. Hydraul. Eng. 130, 38–48. http://dx.doi.org/10.1061/(ASCE)0733-9429(2004)130:1(38).

Tu, J., 2017. Characteristics and Hazard Evaluating of Debris Flow Gullies in Miyun Longtangou Watershed (theses). Beijing Forestry University (in Chinese).

Walczak, N., Walczak, Z., Nieć, J., 2021. Influence of debris on water intake gratings in small hydroelectric plants: An experimental study on hydraulic parameters. Energies 14, 3248. http://dx.doi.org/10.3390/en14113248.

Weller, H., 2002. A Code Independent Notation for Finite Volume Algorithms. Technical Report TR/HGW/02, Nabla Ltd.

Xu, Y., Fan, S., Liu, Y., Zhou, X., Liu, X., Yang, Z., Liu, L., Liu, J., 2016. Analysis of silt interaction with water in an estuary. J. Natural Gas Sci. Eng. 35, 1270–1276. http://dx.doi.org/10.1016/j.jngse.2016.09.035.

Yang, K., Xu, Z.M., Tian, L., Wang, K., Ren, Z., Tang, Y.J., Luo, J.Y., Gao, H.Y., 2020. Significance of coarse clasts in viscous debris flows. Eng. Geol. 272, 105665. http://dx.doi.org/10.1016/j.enggeo.2020.105665.

Yu, D., Tang, L., Chen, C., 2020. Three-dimensional numerical simulation of mud flow from a tailing dam failure across complex terrain. Nat. Hazards Earth Syst. Sci. 20, 727–741. http://dx.doi.org/10.5194/nhess-20-727-2020.

Zalesak, S.T., 1979. Fully multidimensional flux-corrected transport algorithms for fluids. J. Comput. Phys. 31, 335–362. http://dx.doi.org/10.1016/0021-9991(79)90051-2.

Zhang, Y., Chen, J., Tan, C., Bao, Y., Han, X., Yan, J., Mehmood, Q., 2021b. A novel approach to simulating debris flow runout via a three-dimensional CFD code: A case study of Xiaojia gully. Bull. Eng. Geol. Environ. 88, 5293–5313. http://dx.doi.org/10.1007/s10064-021-02270-x.

Zhang, Y., Lu, X.B., Zhang, X.H., 2021d. An optimized eulerian–lagrangian method for two-phase flow with coarse particles: Implementation in open-source field operation and manipulation, verification, and validation. Phys. Fluids 33, 113307. http://dx.doi.org/10.1063/5.0067553.

Zhang, Y., Lu, X., Zhang, X., Li, P., 2021c. Numerical simulation on flow characteristics of large-scale submarine mudflow. Appl. Ocean Res. 108, 102524. http://dx.doi.org/10.1016/j.apor.2021.102524.

Zhang, Y., Ma, C., Yang, H., Ni, S., 2018. Causes and dynamic characteristics of debris flow disaster in longtangou watershed, miyun county of Beijing. J. Beijing For. Univ. 40, 73–84 (in Chinese).

Zhang, R., Su, D., Lei, G., Chen, X., 2021a. Three-dimensional granular column collapse: Impact of column thickness. Powder Technol. 389, 328–338. http://dx.doi.org/10.1016/j.powtec.2021.05.043.

Zhang, Z., Ye, S., Yin, B., Song, X., Wang, Y., Huang, C., Chen, Y., 2021e. A semi-implicit discrepancy model of reynolds stress in a higher-order tensor basis framework for Reynolds-averaged Navier–Stokes simulations. AIP Adv. 11, 045025. http://dx.doi.org/10.1063/5.0033109.

Zhao, E., Dong, Y., Tang, Y., Cui, L., 2021. Numerical study on hydrodynamic load and vibration of pipeline exerted by submarine debris flow. Ocean Eng. 239, 109754. http://dx.doi.org/10.1016/j.oceaneng.2021.109754.